Dilatational rheology of insoluble polymer monolayers: Poly(vinylacetate)

Francisco Monroy, Francisco Ortega, and Ramón G. Rubio*
Departamento de Química Física I, Facultad de Químicas, Universidad Complutense, 28040 Madrid, Spain
(Received 26 February 1998; revised manuscript received 24 July 1998)

The dilatational rheology of the poly(vinylacetate) monolayer onto an aqueous subphase with pH=2.0 has been studied between 1 °C and 25 °C. The combination of several techniques, relaxation after a step compression, oscillatory barrier experiments, electrocapillary waves, and surface light scattering (SLS) by thermal capillary waves, has allowed us to explore a broad frequency range. The relaxation experiments show multiexponential decay curves, whose complexity increases with decreasing the temperature. A regularization technique has been used to obtain the relaxation spectra from the relaxation curves and the dilatational viscoelastic parameters have been calculated from the spectra. The oscillatory barrier experiments confirm the results obtained from the step compression experiments. The dilatational viscosity increases very steeply in the frequency range 0.1–0.001 Hz. The shapes of the relaxation spectra follow the qualitative trends predicted a model recently proposed by Noskov [Colloid Polym. Sci. **273**, 263 (1995)]. The temperature dependence of the fundamental relaxation time follows a Williams-Landel-Ferry equation above 14 °C. These results correspond to the many-chain dynamics regime. The kilohertz region has been explored by the SLS technique. These results are compatible with the existence of a single Maxwell mode, with a relaxation time that has an Arrhenius-type temperature dependence. In the intermediate-frequency regime (10 Hz to 2 kHz) a further Maxwell process is found. It might correspond to the dynamics of loops and tails out of the surface plane. [S1063-651X(98)08012-X]

PACS number(s): 68.10.Et, 05.70.Fh, 62.10.+s, 64.70.Dv

I. INTRODUCTION

Ordered thin organic films with varying thickness from monomolecular layer dimensions (a few nanometers) to multilayer arrays (hundreds of nanometers) are of considerable technological interest in processes such as the fabrication of Langmuir-Blodgett (LB) [1] films or synthetic analogs of biological membranes [2]. It is well known that the starting point of any LB film is a stable fluid monolayer. The ability to optimize the equilibrium and dynamic properties of a given monolayer is determinantal for its successful deposition onto solid substrates. More specifically, Buhaenko and Richardson [3] have clearly shown that the surface rheology of monolayers plays a key role in the LB deposition process.

Despite its obvious importance, neither a theoretical nor a phenomenological framework exists that correlates the equilibrium structural properties with the dynamical rheological ones of monolayers. This is especially important in the case of polymer substances since, when spread onto aqueous subphases, they can form very stiff and extremely viscous monolayers that can be considered as two-dimensional viscoelastic fluids.

If a polymer film is viewed as a macroscopic viscoelastic continuum medium, several types of motion are possible [4]. As shown in Fig. 1, we may distinguish two main types: capillary (or out of plane) and dilatational (or in plane) [5]. The first one is a shear deformation, while for the second one there are both a compression-dilatation motion and a shear motion. Since dissipative effects do exist within the film, each of the motions consists of elastic and viscous components. The elastic constant for the capillary motion is the surface tension γ, while for the second it is the dilatation elasticity ϵ. The latter modulus depends upon the stress applied to the monolayer. For a uniaxial stress (as it is the case for capillary waves or for compression in a single barrier Langmuir trough) the dilatational modulus is the sum of the compression and shear moduli [6]

$$\tilde{\varepsilon}_K = K + i\omega\eta_k, \tag{1}$$

$$\tilde{\varepsilon}(\omega) = \tilde{\varepsilon}_k + \tilde{\varepsilon}_s = \varepsilon_R + i\omega\kappa,$$

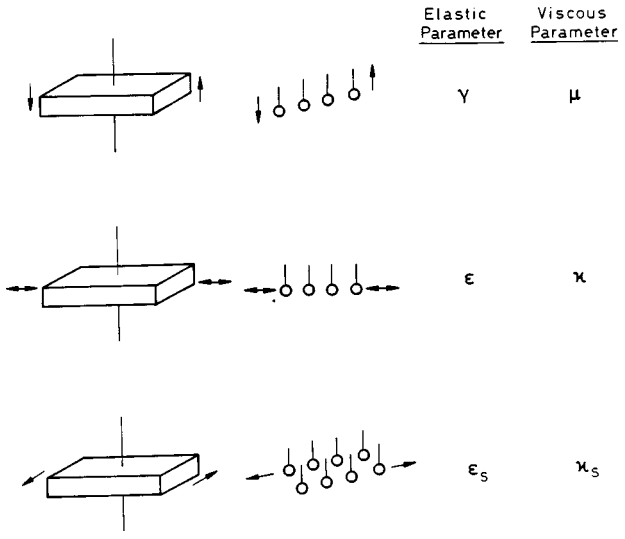

FIG. 1. Sketch of different surface relaxation modes and the corresponding viscoelastic parameters. Adapted from Kawaguchi [5].

*Author to whom correspondence should be addressed.
Electronic address: RGRUBIO@eucmax.sim.ucm.es

$$\tilde{\varepsilon}_S = S + i\omega\eta_s,$$

where ω denotes the angular frequency and the $\omega\eta$'s are the loss components of the compression and shear motions. Hereinafter we will refer to ε and κ as the dilatational elasticity and viscosity, respectively.

Shear viscosity has certainly been the most intensively investigated property [4,7]. Although dilatational viscoelasticity seems rather to be the dominant property in interfacial hydrodynamics [8], there are relatively few studies on dilatational properties of insoluble monolayers over broad frequency ranges.

There are several experimental techniques suitable for studying $\tilde{\varepsilon}$. In the present work we will make use of four: (a) relaxation after a sudden compression of the monolayer, (b) an oscillatory barrier, (c) electrocapillary waves, and (d) light scattering by thermally excited capillary waves. The first two techniques will be used in the low-frequency range (below 1 Hz), the third between 10 Hz and 1 kHz, and the last one in the kilohertz range.

The rest of this paper is organized as follows. Section II gives experimental details of the chemicals and the experimental techniques. Section III contains the results and a discussion. Finally, Sec. IV summarizes the main conclusions.

II. EXPERIMENT

A. Chemicals

Poly(vinylacetate) was purchased from Polysciences (Germany). It had a Molecular weight of 90.000 and a polydispersity index of 1.3. Test experiments with a monodisperse sample (polydispersity index 1.03) lead to comparable results. The spreading solution was a mixture of benzene plus tetrahydrofurane (5:1) and had a concentration close to $10^{-3}M$. The solvents were purchased from Carlo Erba (RPE quality, Italy). Before preparing the polymer solutions, the surface tension of the solvents was measured by the plate method in order to be sure that they did not have significant amounts of surface active impurities. Good agreement was found between the values measured and those reported by Jasper [9]. Before preparing the spreading solution, the polymer was dissolved in tetrahydrofurane and filtered through 0.5-μm Teflon membranes. Double distilled and deionized water from a Milli$Q$-RG system was used. Its resistivity was always higher than 18 MΩ cm^{-1}. The subphase of pH$=2.0$ was obtained by adding a ClH solution (Aldrich, USA).

B. Langmuir trough

The monolayers were formed on a commercially available Teflon Langmuir trough (KSV Instruments Minitrough, Finland) with a computerized control. A Pt-Wilhelmy balance was used as a surface pressure sensor. Polyoxymethylene (Delrin) barriers were used. The whole setup was enclosed in a box through which a small flow of filtered N_2 was maintained. A Petry cell containing subphase was placed inside the box in order to keep the humidity level. The temperature control of water in the trough was carried out by passing thermostated water into the jacket at the bottom of the trough. The temperature near the surface was measured with a calibrated Pt-100 sensor. The temperature of the box was kept constant within $\pm 0.1°$ at the same temperature of the measurements. The box has two optical windows for the light-scattering experiments.

For the equilibrium measurements, the spreading solution was slowly applied by a microsyringe at different places onto the surface. The surface concentration was changed by subsequent additions of the polymer solution. Times ranging from 15 to 50 min were allowed for solvent evaporation and equilibration. The surface pressure Π was continuously monitored and the equilibrium value was taken only when Π remained constant for at least 20 min. The surface of the subphase was swept with the barriers until the expected surface tension was obtained. In order to ensure that the spreading solvent did not add any significant impurities, blank experiments with the solvent were done before forming a monolayer.

Each reading of the surface pressure was determined within ± 10 μN/m, although the repetitivity under small cyclic changes of the position of the barriers was around ± 30 μN/m. The stability of the subphase temperature was better than $\pm 0.05°$.

C. Step-compression experiments

The step-compression experiments were carried out in the Langmuir trough by moving the barrier under computer control after the desired surface concentration Γ_s had been reached and the equilibrium value of Π obtained. In these experiments the area change ΔA was kept below 10% of the total area. The time necessary to make such change was slightly less than 1 s. Readings at constant intervals of 1 s were taken until the equilibrium value of Π at the final value of the area was reached. A relaxation curve was acceptable only if the initial and final values of Π were in agreement with the corresponding equilibrium values. The results reported are the average of at least three relaxation curves that agree within their combined experimental uncertainties.

D. Oscillatory barrier experiments

These experiments were carried out by inducing an oscillatory movement at the barrier. They were performed at constant barrier speed and the frequency was varied by changing the maximum area change ΔA. In our setup $\Delta A/A_0$ ranged from 0.2% to 12%, A_0 being the initial area. For an experimental result to be accepted, the values of Π at the minimum and maximum values of the monolayer area had to coincide with the corresponding equilibrium values within their combined uncertainties.

E. Electrocapillary waves

The technique used is similar to that described by Ito *et al.* [10] and Jayalakshmi, Ozanne, and Langevin [11]. In this technique surface capillary waves in the frequency range 20 Hz to 2 kHz are produced at the air-liquid interface upon application of an ac electric field through a blade positioned within 100 μm of the interface. The spatial wave vector q and the corresponding wave damping coefficient α for the capillary waves produced are determined by measuring the optical diffraction of a laser beam positioned at various distances from the blade. The phase difference and amplitude

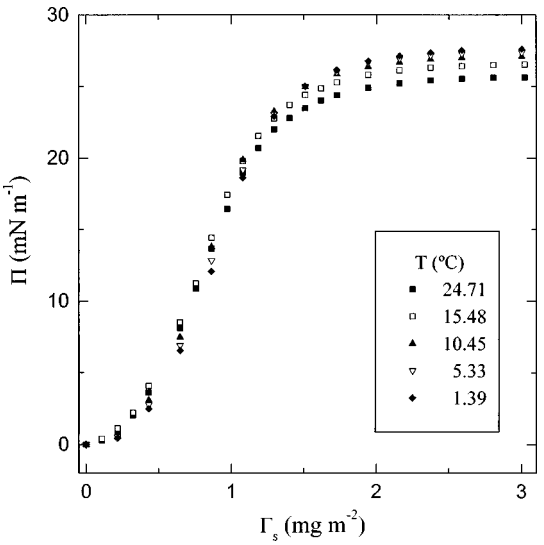

FIG. 2. Surface pressure isotherms for PVAC onto an aqueous subphase with $p\mathrm{H}=2.0$. Notice that the isotherms cross each other at $\Gamma_s \approx 1$ mg m^2.

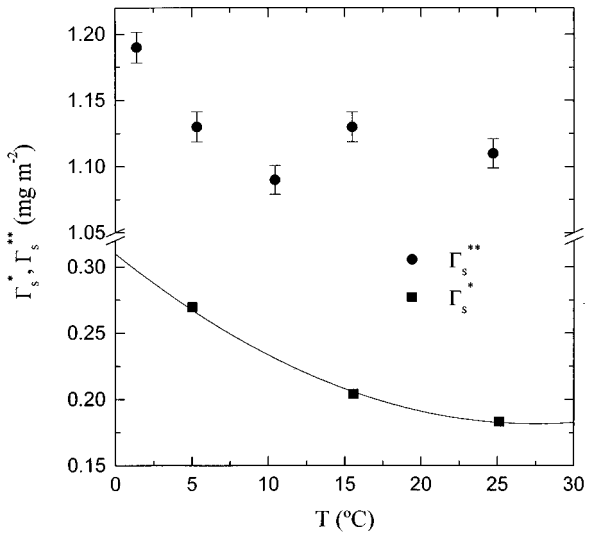

FIG. 3. Temperature dependence of the surface concentrations that mark the transitions from dilute to semidilute (Γ^*) and from semidilute to concentrated (Γ^{**}) regimes.

ratio as a function of distance give rise to q and α. These two parameters are then used to obtain the elasticity and dilatational viscosity from the dispersion equation [12,13]. The instrument was calibrated by determining the surface tension of water.

F. Surface light-scattering experiments

The surface light-scattering setup is similar to the one described by Earnshaw and McGivern [14], Richards, Rochford, and Taylor [15], and Kolevzon and Gerbeth [16]. A polarized 25-mW He-Ne laser beam passes through a spatial filter that expands the beam and gives a clean Gaussian intensity profile. Then the beam passes through a transmission diffraction grating from Alingn-Rite (USA) with nine different patterns. In all the experiments reported we have used one with 5-μm-wide dark lines, each spaced 275 μm from each other. A 1:1 image of the grating is formed onto the monolayer by means of a focusing lens. The light scattered by the capillary waves is detected in the heterodyne mode, mixed with the light reflected by a diffracted beam. The wave vector is selected by focusing each of the diffraction spots in the photomultiplier. The signal is collected and analyzed by a NICOM (USA) model 170 autocorrelator. The spectrometer has been calibrated using simple liquids (n-hexane, ethanol, and water) and can be used in the wave-vector range $100 \leqslant q/\mathrm{cm}^{-1} \leqslant 900$.

III. RESULTS AND DISCUSSION

A. Equilibrium results

Figure 2 shows the Π-Γ curves for poly(vinylacetate) (PVAC) onto aqueous subphase ($p\mathrm{H}=2.0$) at different temperatures. Experiments carried out onto a water subphase ($p\mathrm{H}=7.0$) at 25 °C lead to results that were coincident with those of Yoo and Yu [17]. It can be observed that for surface concentrations $\Gamma < 1.5$ mg m^{-2} $(\partial\Pi/\partial T)_\Gamma < 0$, while at higher concentrations it is positive. This behavior is similar to that reported by Yoo and Yu [17] between 15 °C and 30 °C and for $p\mathrm{H}=7.0$. From the data in Fig. 3 it is possible to calculate the surface entropies and enthalpies, which are positive at low values of Γ_s and negative at high ones.

From the low-Π regions of the isotherms it has been possible to calculate the critical exponent of the radius of gyration ν for PVAC [18]. Within the experimental uncertainty ν remains constant at 0.78 ± 0.03 over the whole temperature range. This value is in excellent agreement with the value obtained in Ref. [18] for the same polymer onto a subphase with $p\mathrm{H}=7.0$ and with the prediction of the renormalization group for polymer in good solvents. Therefore, we can conclude that the aqueous ($p\mathrm{H}=2.0$)-air interface is a good solvent for PVAC over the whole temperature range studied.

We have also been able to calculate the concentrations that mark the crossover from dilute to semidilute Γ^* and from semidilute to concentrate regimes Γ^{**}. Figure 3 shows that Γ^* decreases monotonically with increasing T, reflecting the tendency of the chains to be more expanded in the monolayer. However, the behavior of Γ^{**} is less clear due to the larger uncertainties associated with their values.

From the Π-Γ curves it is possible to calculate the static elasticity modulus

$$\varepsilon_s = \left(\frac{\partial \Pi}{\partial \ln \Gamma} \right)_T , \tag{2}$$

which would correspond to the $\tilde{\varepsilon}$ defined in Eq. (1) for an instantaneous deformation of the monolayer and therefore without any dissipative effects. Figure 4 shows ε_s at 25 °C. It can be observed that most of the increase of the elasticity takes place within the semidilute regime. The techniques for the different type of dynamical experiments have different requirements about the values of ε_s at which the precision is better. It must also be recalled that deposition of monolayers by the Langmuir-Blodgett technique is usually done in states of relatively high values of Γ_s [1].

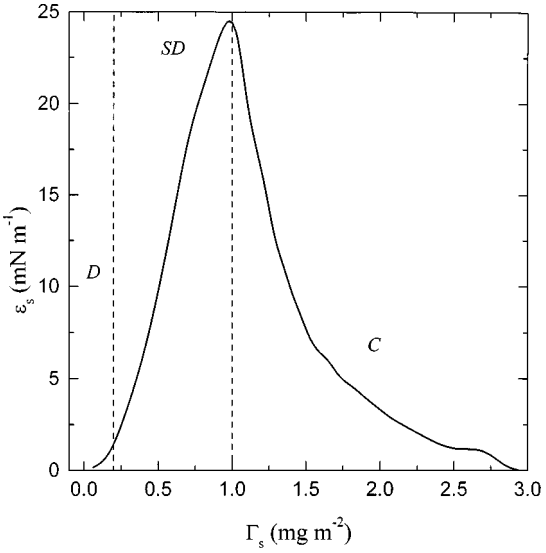

FIG. 4. Static compressibility modulus $\varepsilon = d\Pi/d \ln \Gamma_s$ at 25 °C, calculated from the Π vs Γ_s curve. The dashed lines indicate the limits of the dilute (*D*), semidilute (SD), and concentrated regimes (*C*).

B. Dynamical experiments

Loglio, Tesei, and Cini [19] showed that for systems not too far from equilibrium, when nonlinear processes (e.g., convection) are not present, the complex elasticity modulus can be written as

$$\tilde{\varepsilon}(\omega) = \frac{\mathcal{F}\{\Delta\gamma(t)\}}{\mathcal{F}\{\Delta A/A_0\}} = \frac{\mathcal{F}\left\{\dfrac{d\Delta\gamma(t)}{dt}\right\}}{\mathcal{F}\left\{\dfrac{d \ln A(t)}{dt}\right\}}, \tag{3}$$

where $\mathcal{F}$ denotes Fourier transform and γ is the surface tension. Joos and Van Uffelen [20] have recently shown that Eq. (3) has to be taken with care for soluble monolayers in experiments in which *A* changes continuously with *t*. Since PVAC is not soluble, Eq. (3) is valid as far as the maximum value of $\theta = \Delta A/A_0$ is not high (below 10% for most of our experiments).

1. Step-compression experiments

For a fast change of area, one can write

$$\mathcal{F}\left\{\frac{\Delta A}{A_0}\right\} = i\omega \frac{\Delta A}{A_0} = i\omega\theta, \tag{4}$$

which leads to

$$\tilde{\varepsilon}(\omega) = \frac{i\omega}{\theta} \int_0^\infty \Delta\gamma(t)\exp(-i\omega t)dt. \tag{5}$$

$\Delta\gamma(t)$ has been frequently written as [21]

$$\Delta\gamma(t) = \sum_1^n (\Delta\gamma)_i^0 \exp(-it/\tau_i), \tag{6}$$

thus leading to

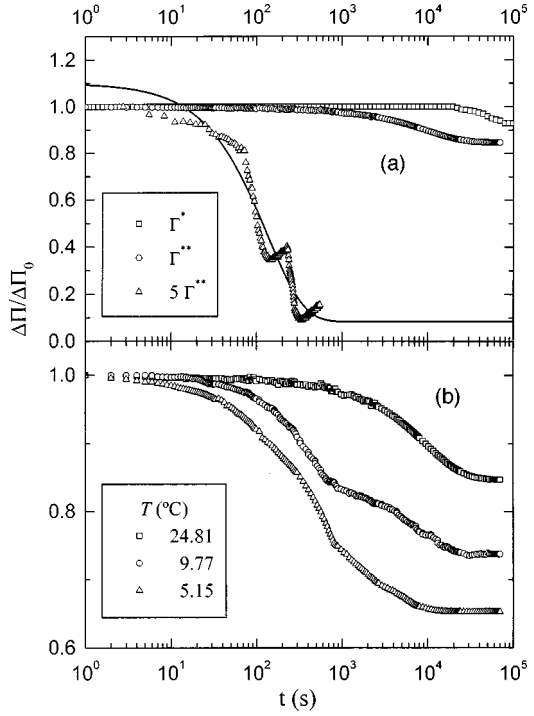

FIG. 5. Examples of relaxation curves in the step-compression experiments. (a) Relaxation curves for three initial values of Γ_s. Notice that for $\Gamma_s = 5\Gamma^{**}$ the curve shows several steps that arise from the fact that the monolayer has been driven into the collapse state during the compression. (b) Relaxation curves for $\Gamma_s = \Gamma^{**}$ at three different temperatures. Notice that the complexity of the structure of the curves increases with decreasing *T*.

$$\theta\tilde{\varepsilon}(\omega) = \sum_{i=1}^n \varepsilon_i^0 \frac{i\omega\tau_i}{1+i\omega\tau_i}. \tag{7}$$

This means that, in general, $\tilde{\varepsilon}(\omega)$ can be expressed as a sum of Maxwell processes.

Figure 5(a) shows the relaxation curves obtained at 25 °C for three different surface concentrations: $\Gamma_s \approx \Gamma^*$, Γ^{**}, and $5\Gamma^{**}$. It can be observed that, as expected, the relaxation is faster for Γ^{**} than for Γ^*. We have included the relaxation curve corresponding to a single exponential decay and it can be seen than even for the lowest concentration the relaxation is more complex than a single Maxwell mode. It can also be seen that for $5\Gamma^{**}$ the relaxation curve presents several peaks. It is worth mentioning that for Γ^* a large induction period appears in which the decrease of Π is relatively slow. It should also be noticed that very large times are required for a complete relaxation of the monolayer.

Figure 5(b) shows the relaxation curves at three different temperatures for Γ^{**}. As in the previous case, one observes the induction period followed by a complex decay of the surface pressure. In general, it has been found that the complexity of the relaxation curves increases with decreasing *T*.

Since there is no *a priori* way to know the number of exponentials needed in Eq. (6) in order to describe the present relaxation curves with random distribution of errors, we have followed a different approach. It is known that a relaxation curve is related to the relaxation spectrum $H(\ln\tau)$ [22]. In our case, one can write

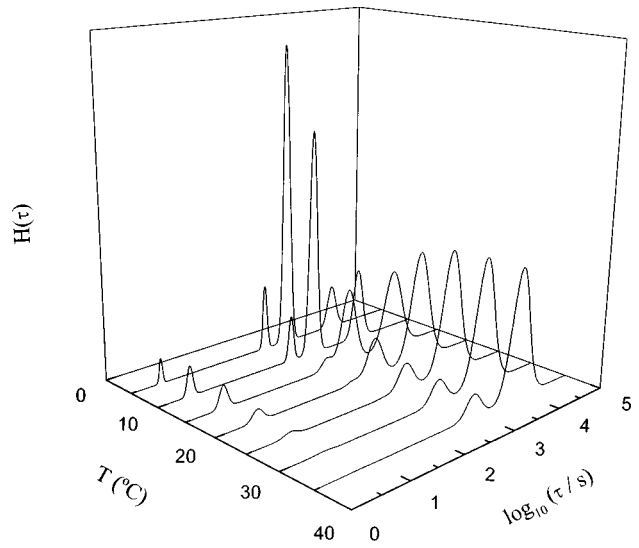

FIG. 6. Relaxation spectra for monolayers with $\Gamma_s=\Gamma^{**}$ at different temperatures.

$$\Delta\Pi/\Pi_0=\int_{-\infty}^{\infty}H(\ln\ \tau)\exp(-t/\tau)d\ \ln\ \tau, \tag{8}$$

where $\Pi_0=\Pi(t=0)$. In order to carry out the inverse Laplace transform necessary to obtain $H(\ln\tau)$ from the $\Pi(t)$ curves, we have used an algorithm based on Tikhonov's regularization method, as described by Jakes [23]. A good definition of the spectrum can be obtained since both plateaus at short and long times are well defined in the experimental relaxation curves. The results are shown in Fig. 6. Table I gives the relaxation times corresponding to each relaxation process (peak) in $H(\ln\tau)$ and their corresponding amplitudes for the normalized spectrum: $\int_{-\infty}^{\infty}H(\ln\tau)d\ln\tau=1$. For reasons to be discussed below, we have assigned an odd integer number p to each of the peaks of the spectrum, with $p=1$ corresponding to the process with the largest relaxation time. It can be observed that decreasing T increases the weight (amplitude) of the faster relaxation processes, therefore confirming the increase of the complexity of the relaxation curves. However, it is important to notice that the amplitude of the slowest mode becomes negligible below approximately 14 °C, where it cannot be observed any longer. This will be discussed below.

Once $H(\ln\tau)$ is obtained, both the real and the imaginary components of the elasticity can be calculated through

$$\varepsilon_R=\frac{1}{\theta}\int_{-\infty}^{\infty}H(\ln\ \tau)\ \frac{\omega^2\tau^2}{1+\omega^2\tau^2}\ d\ \ln\ \tau, \tag{9}$$

$$\varepsilon_I=\omega\kappa=\frac{1}{\theta}\int_{-\infty}^{\infty}H(\ln\ \tau)\ \frac{\omega\tau}{1+\omega^2\tau^2}\ d\ \ln\ \tau. \tag{10}$$

Figure 7(a) shows the results obtained at 25 °C for three values of Γ_s within the semidilute regime. It can be observed that the complexity of the relaxation process increases with Γ_s since the relative weight of the slowest mode decreases [see the $\varepsilon_I(\omega)$ curves in the figure]. The dilatational viscosity curves show that the low-frequency limit of κ increases with Γ_s, as it has been frequently found for the shear viscosity in experiments performed with torsion pendulums [24]. More interestingly, one can observe a dramatic increase of κ as the frequency decreases, reaching the Newtonian limit behavior at low frequencies if Γ_s is increased. For the frequency range $0.1-10^{-4}$ Hz, the overall slope of $\log_{10}(\kappa)$ vs $\log_{10}(\omega)$ in all the monolayer states measured ranges be-

TABLE I. Relaxation times τ_i and relative amplitudes A_i of the different modes in the relaxation spectra obtained from step-compression experiments at the temperatures studied. The type 2 mode corresponds to the fast adsorption-desorption mode in Noskov's model. Type 3 modes correspond to the reptation process and p_i's denote the odd-integer numbers corresponding to the Fourier components in which the overall reptation dynamics is decomposed in Noskov's model.

		Type 2		Type 3		
T (°C)		$p_2=1$	$p_3=7$	$p_3=5$	$p_3=3$	$p_3=1$
1.05 ± 0.10	τ_i (s)	3.2 ± 0.8		50 ± 1	$(6.0\pm0.3)\times10^2$	$(7.1\pm0.3)\times10^3$
	A_i^0	0.007		0.144	0.717	0.132
5.15 ± 0.12	τ_i (s)	3.3 ± 1.2		69 ± 2	$(5.7\pm0.2)\times10^2$	$(7.0\pm0.3)\times10^3$
	A_i^0	0.015		0.132	0.692	0.161
9.77 ± 0.10	τ_i (s)	3.5 ± 0.2		127 ± 2	$(6.0\pm0.5)\times10^2$	$(6.7\pm1.7)\times10^3$
	A_i^0	0.070		0.087	0.538	0.305
15.36 ± 0.10	τ_i (s)	4.4 ± 0.6	40 ± 5	213 ± 50	$(8.4\pm3.0)\times10^2$	$(8.8\pm7.0)\times10^3$
	A_i^0	0.049	0.008	0.072	0.273	0.598
17.20 ± 0.08	τ_i (s)	4.8 ± 0.5	62 ± 10	223 ± 45	$(8.2\pm2.0)\times10^2$	$(8.2\pm0.5)\times10^3$
	A_i^0	0.045	0.004	0.067	0.189	0.695
20.10 ± 0.07	τ_i (s)	5.2 ± 0.7		242 ± 40	$(8.0\pm2.0)\times10^2$	$(7.8\pm1.0)\times10^3$
	A_i^0	0.037		0.057	0.091	0.815
24.81 ± 0.07	τ_i (s)	5.6 ± 1.3		238 ± 50	$(7.9\pm1.3)\times10^2$	$(7.7\pm0.5)\times10^3$
	A_i^0	0.025		0.013	0.036	0.926
30.10 ± 0.10	τ_i (s)	5.7 ± 1.0		260 ± 70	$(8.0\pm2.0)\times10^2$	$(7.5\pm0.5)\times10^3$
	A_i^0	0.012		0.008	0.030	0.950

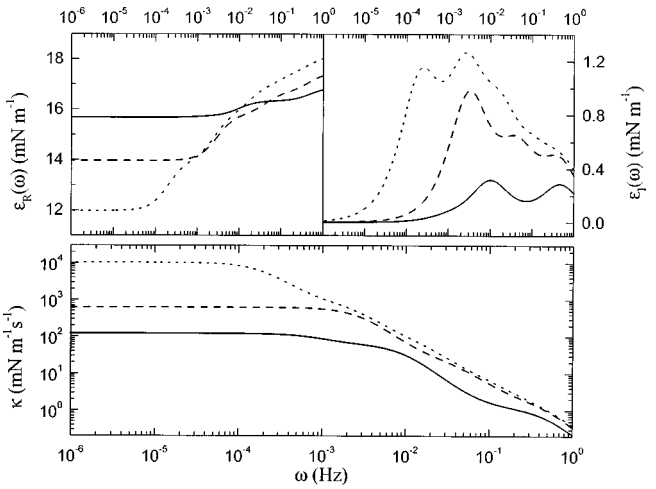

FIG. 7. (a) Real and imaginary components of the elastic modulus $\tilde{\varepsilon}(\omega)=\varepsilon_R+i\varepsilon_I=\varepsilon_R+i\omega\kappa$ and the corresponding dilatational viscosity. The curves have been calculated from the relaxation spectra shown in Fig. 6, with the parameters of Table I. The lines correspond to different temperatures: ——, 25 °C; − − −, 10 °C; and · · · ·, 5 °C.

tween −0.9 and −1.1. This value is very similar to the slope of the viscosity vs shear rate for polymers between two close plates [25].

The effect of T on κ can be observed in Fig. 8. There is a steady decrease in the low-frequency limit of κ associated with the higher values of Π at higher temperatures. At frequencies higher than 10^{-4} Hz the situation is less clear and reflects the increasing importance of the faster relaxation modes as T decreases. The large difference observed between the isotherms of 25 °C and 10 °C is due to the fact that the mode with the largest relaxation time disappears.

The relatively large number of relaxation modes collected in Table I for each relaxation curve and the fact that the value of the lowest relaxation time is not very high in comparison to the time of the step compression make it necessary

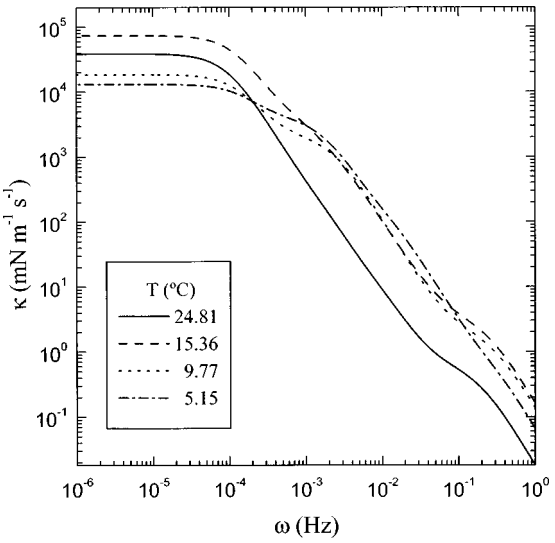

FIG. 8. Frequency and temperature dependence of the dilatational modulus for monolayers with $\Gamma_s\approx\Gamma^{**}$. In all the cases the slope of the κ-decreasing section roughly corresponds to −1.

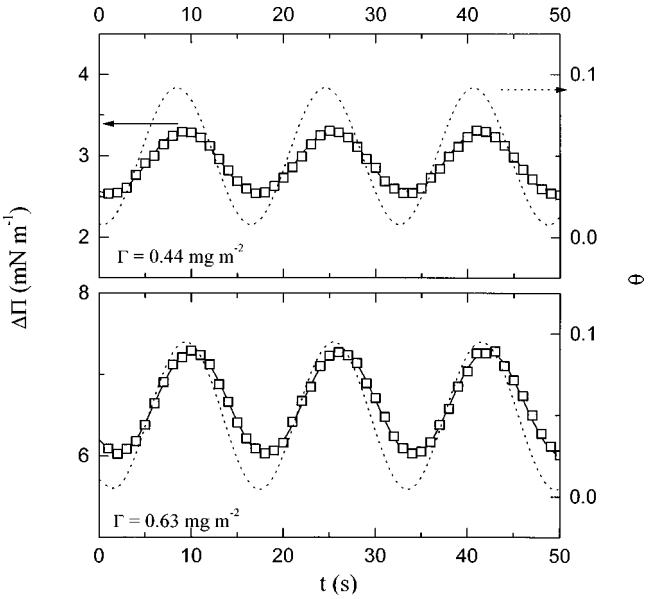

FIG. 9. Typical outputs of oscillatory-barrier experiments for two initial surface concentrations at 25 °C. In both cases the speed of the barriers was adapted in such a way that $\max(\Delta A/A_0)\leqslant 0.1$.

to carry out some further test in order to confirm the structure of $H(\ln\tau)$. The oscillatory barrier experiments are adequate for this purpose.

2. Oscillatory barrier experiments

In this type of experiment the change of area has the time dependence

$$A=A_0\exp(-i\omega t), \tag{11}$$

which leads to an elasticity modulus (for linear processes) [22]

$$\tilde{\varepsilon}(\omega)=\varepsilon_R+i\omega\kappa=|\varepsilon|\exp(i\phi), \tag{12}$$

with

$$|\varepsilon|=[\varepsilon_R^2+\omega^2\kappa^2]^{1/2},\quad \tan\phi=\frac{\omega\kappa}{\varepsilon_R}. \tag{13}$$

Experimentally, one follows the change of Π with A and $\tilde{\varepsilon}(\omega)$ can be calculated through

$$\tilde{\varepsilon}(\omega)=\left[\frac{\Delta\Pi(\omega)}{\theta(\omega)}\right]_T=\frac{\Delta\Pi_0}{\theta_0}\exp(i\varphi), \tag{14}$$

where $\Delta\Pi_0$ is the total change in surface pressure for a semiperiod of the barrier motion and θ_0 is the total relative change in area for the same semiperiod. φ is the phase lag between the curves that give the values of Π and θ. Figure 9 shows typical results at 25 °C for two values of $\Pi(t=0)$. A comparison of Eqs. (12) and (14) shows how to relate ε_R and κ with $\Delta\Pi_0/\theta_0$ and φ.

Frequency-dependent measurements can be done by moving the barrier at constant velocity and changing θ_0. Figure 10 shows the results obtained at 25 °C between 0.2 and 2 Hz, corresponding to values of θ_0 between 2% and 12%. In all the cases the starting surface concentration was Γ^{**}. Mea-

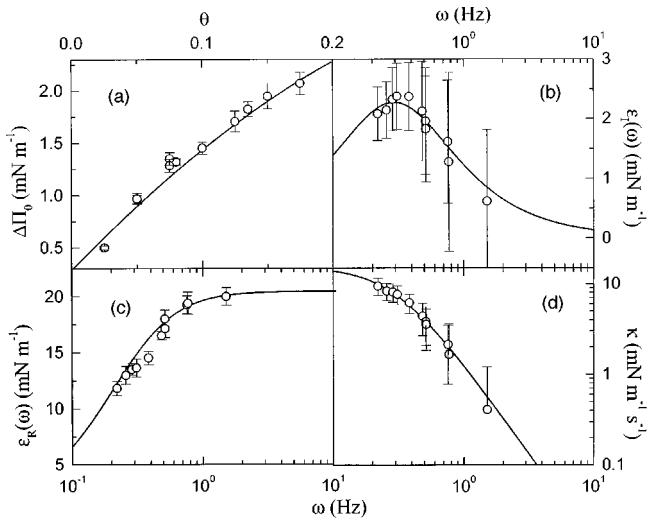

FIG. 10. Viscoelastic parameters obtained from oscillatory-barrier experiments at 25 °C. $\Delta\Pi_0$ represents the change in surface pressure between the two extreme positions of the barrier. The continuous curve in (a) has been calculated from the equilibrium isotherms. The curves in (b)–(d) have been calculated from a Maxwell relaxation mode with the relaxation time corresponding to the fastest mode of the relaxation spectrum obtained in the step-compression experiments (Table I).

surements at lower frequencies have not been done since it is necessary to ensure that the velocity of the concentration wave induced by the barrier is much higher than the velocity of the barrier itself [26]. The velocity of the surface wave grows with both ω and $|\varepsilon|$.

Figure 11(a) shows the values of $\Delta\Pi_0$ for different values of θ_0. The curve represents the values calculated from the equilibrium Π-Γ_s curve. The agreement indicates that no irreversible process has been introduced by the motion of the barrier. Figures 11(b)–11(d) show the real and imaginary components of the elasticity and the corresponding viscosity. The curves are the predictions of a Maxwell process with the relaxation time taken from Table I [$\tau=(2.4\pm0.5)\times10^2$ s]. Similar agreement has been found at all the temperatures.

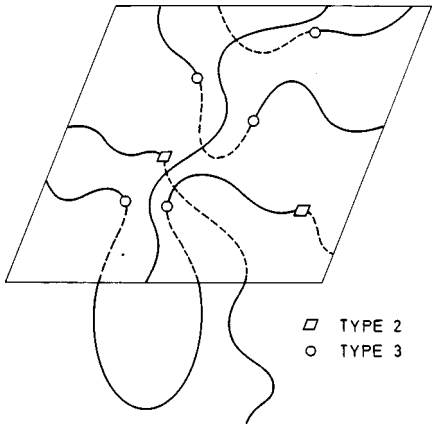

FIG. 11. Sketch of an insoluble polymer monolayer according to Noskov's model. The lines represent the polymer chains that may cross the monolayer plane at one point (□) or at two points (○). The crossing points define a two-dimensional channel along which other chains may reptate.

These results confirm the validity of the results obtained in Sec. III B 1 using the regularization method.

3. Comparison with Noskov's model

Noskov has proposed a rheological model to describe the elasticity of polymer monolayers [27]. As is sketched in Fig. 11, parts of the polymer chains are adsorbed onto the subphase, while other parts form loops or tails protruding in either adjacent phase. The points at which the chains cross the monolayer plane define channels through which other chains move. The model considers two main contributions to the dynamics of the polymer chains: first, the reptation of polymer chains through the two-dimensional channels and, second, the adsorption and desorption of chain blobs onto the surface.

After suitable physical and mathematical approximations, Noskov arrived at the expression for the elasticity modulus [27]

$$\tilde{\varepsilon}(\omega)=-\left(\frac{\partial\gamma}{\partial\ln\Gamma}\right)\left\{\frac{16\Gamma_3}{\pi^3\Gamma_s}\sum_{p,\mathrm{odd}}\frac{i\omega\tau_p}{1+i\omega\tau_p}+\left(1-\frac{2\Gamma_3}{\pi\Gamma_s}\right)\frac{i\omega\tau_2}{1+i\omega\tau_2}\right\},\tag{15}$$

$$\tau_p=\frac{\tau_B}{p^2},$$

where Γ_3 refers to the surface concentration of trains with two crossing points at the monolayer plane, i.e., loops. p is an integer odd number, τ_B is the characteristic time for intramolecular motion along the primitive chain within the tube, and τ_2 is the relaxation time characteristic of the squeezing out (drawing in) the chains of the monolayer [27]. It must be said that among the approximations made in the model, it is assumed that (a) the chains are long enough to consider that the number of loops greatly exceeds the number of tails, (b) the concentration of transitional points is much smaller than the concentration of monomers adsorbed (not very high surface pressures), and (c) $\tau_2>\tau_B$.

Equation (15) indicates that $\tilde{\varepsilon}(\omega)$ is given by the static value $\varepsilon_s=(\partial\gamma/\partial\ln\Gamma_s)$ corrected by two main contributions: a Maxwell mode arising from the adsorption process from the adjacent bulk phases and a multitude of Maxwell modes arising from the relaxation of the chains in the monolayer plane. As is shown by Eq. (15), the relaxation times of the latter modes are all related to τ_B. Table I shows the values of p assigned to the different relaxation times obtained in the step-compression experiments. Figure 12 shows that the different relaxation times do not follow exactly Eq. (15) at all the temperatures, but they are well described by $\tau_p=\tau_B/p^\delta$, with δ being a function of T, at least for temperatures above 15 °C. It must also be pointed out that, in general, the values of τ_p corresponding to the highest values of p tend to lie below the straight line.

Figure 13 shows the temperature dependence of τ_B derived from Eq. (15). The curve corresponds to a fit to the Williams-Landel-Ferry equation [28]

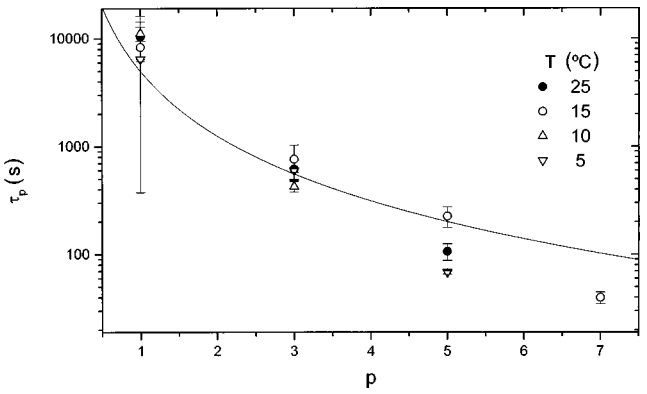

FIG. 12. Relaxation times characteristic of the modes of the relaxation spectra as a function of the odd-integer index p. The full line represents the slope predicted by the reptation dynamics used in Noskov's model.

$$\ln \tau_B(T) = \ln \tau_B(T_0) - \frac{C_1(T-T_0)}{C_2+T-T_0}, \tag{16}$$

with the ratio $C_2/C_1 = 3$ K, corresponding to the ''universal'' values given in [28]. The value $T_0 = 287 \pm 1$ K roughly corresponds to the temperature at which the peak corresponding to the slowest mode in the spectrum $H(\ln \tau)$ is no longer detected. Below T_0, τ_B takes much lower values and again slowly increases with decreasing T. It must be recalled that our PVAC sample has a bulk glass transition temperature, $T_g \approx 317$ K and for this type of quasi-two-dimensional system it is expected that the polymer chains will have a larger mobility and hence a lower T_g.

4. Electrocapillary waves

Figure 14 shows the values of the wave vector q and damping α obtained at 25 °C for two values of the surface concentration $\Gamma = 0.5$ mg m^{-2} and $\Gamma = 1.0$ mg m$^{-2} \approx \Gamma^{**}$. The elasticity and viscosity were estimated from the dispersion equation [12,13]

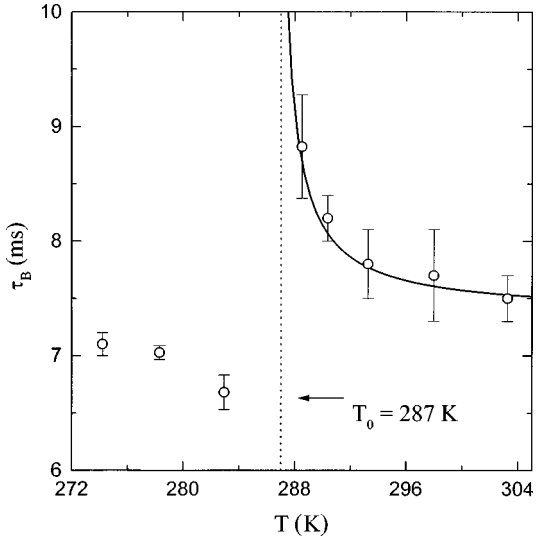

FIG. 13. Temperature dependence of the basic relaxation time τ_B in Noskov's model. The line is a fit to the Williams-Landel-Ferry equation with a characteristic temperature $T_0 = 287$ K.

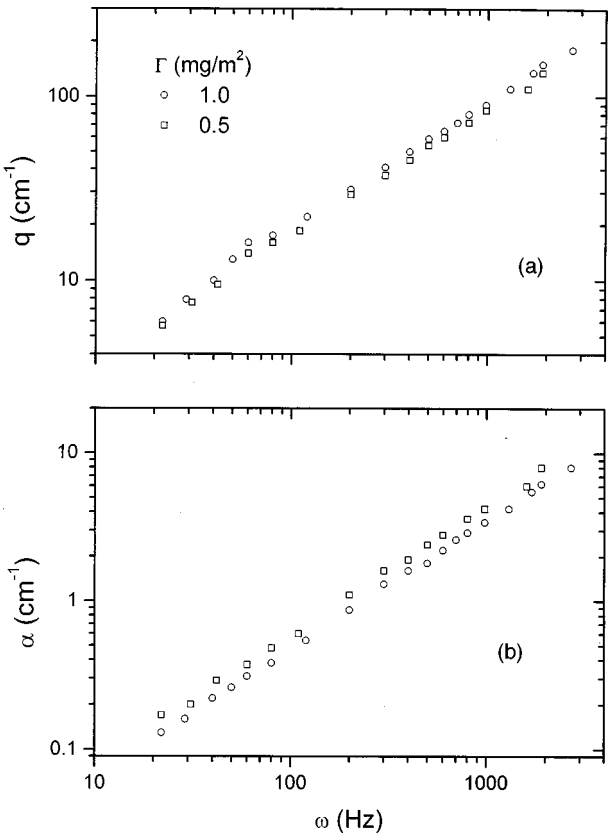

FIG. 14. (a) Wave vector q and (b) damping α of the electrocapillary waves for two values of the surface concentration at 25 °C. Notice that $\Gamma = 1.0$ mg m^{-2} is very close to Γ^{**}.

$$\left[\frac{\tilde{\varepsilon}\tilde{q}^2}{\omega} + i\eta(\tilde{q}+m) i\eta'(\tilde{q}+m')\right] \times \left[i\eta(\tilde{q}+m) + i\eta'(\tilde{q}+m') + \frac{\tilde{\gamma}\tilde{q}^2}{\omega} + \frac{g(\rho-\rho')}{\omega} - \frac{\omega(\rho+\rho')}{\tilde{q}}\right] + [\eta(\tilde{q}+m) - \eta'(\tilde{q}-m')]^2 = 0, \tag{17}$$

where $\tilde{q} = q - i\alpha$, $m \equiv [\tilde{q}^2 + (i\omega\rho/\eta)]$, $m' \equiv [\tilde{q}^2 + (i\omega\rho'/\eta')]$, ω is the angular frequency, g is the gravity constant, η and η' are the shear viscosities of air and subphase, respectively, and ρ and ρ' are the densities of air and subphase, respectively. $\tilde{\varepsilon} = \varepsilon_R - i\omega\kappa$, where ε_R is the dynamic elasticity and κ the dilatational viscosity. $\tilde{\gamma} = \gamma - i\omega\mu$, where γ is the dynamic surface tension and μ is the transverse viscosity. Following Sauer *et al.* [29] and Gau, Yu, and Zografi [12] we have assumed $\mu = 0$ and $\tilde{\gamma} = \gamma$; for the latter we have used the static values.

Figure 15 shows the values of $\varepsilon(\omega)$ and $\omega\kappa(\omega)$ for $\Gamma \approx \Gamma^{**}$. As can be observed, there is a further relaxation process centered around 100 kHz. The existence of this process does not seem to correspond to the series of modes corresponding to the collective reptation observed in the previous relaxation experiments. Similar relaxation phenomena have been found for soluble monolayers of hydroxyethylcellulose and hydroxypropylcellulose in the same frequency range [12]. The main differences between the viscoelastic behavior

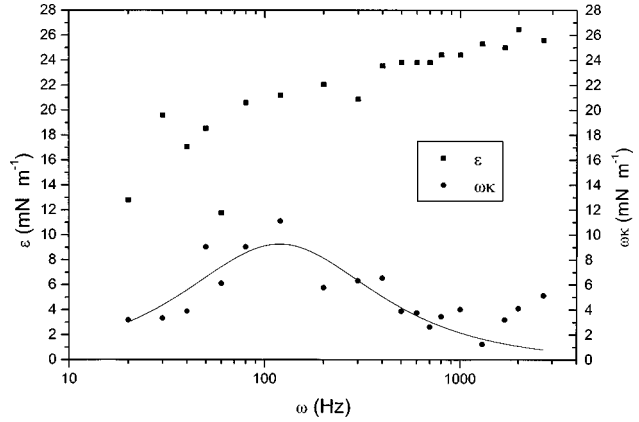

FIG. 15. Real and imaginary components of the elasticity modulus obtained from the electrocapillary wave data for $\Gamma \approx \Gamma^{**}$ and 25 °C. The line corresponds to the best fit of the $\omega\kappa$ data to a Maxwell mode with relaxation time 8.5 ± 0.7 ms.

of these two polymers were assigned to the different solubility of the two polymers in the subphase and therefore to differences in their adsorption-desorption dynamics. As already mentioned, this process is an important ingredient in Noskov's model and does not have a direct correspondence with the viscoelastic regimes usually described in three-dimensional polymer systems: collective reptation dynamics at low frequencies and high-frequency Rouse-like dynamics.

5. Surface light scattering

(a) Basic equations. Thorough descriptions of the theory of surface quasielastic light scattering are given by Langevin [30]. Capillary fluctuations are described as displacements of the fluid surface from its equilibrium plane by the equation

$$d(r,t) = d_0 \exp[i(qx + \omega t)], \tag{18}$$

where q is the surface wave number of the capillary wave that has a frequency ω and propagates in the x direction. The frequency is a complex quantity that describes the time evolution of the surface due to fluctuations of frequency ω_0, which are subject to a decay process with a damping constant Θ,

$$\omega = \omega_0 + i\Theta. \tag{19}$$

The dispersion relation between ω and q for a fluid surface covered by an insoluble monolayer is given by [30,31]

$$\begin{aligned} D(\omega) = {} & [\tilde{\varepsilon} q^2 + i\omega\eta(q+m)] \\ & \times [\tilde{\gamma} q^2 + i\omega\eta(q+m) + g\rho - \omega^2\rho/q] \\ & - [i\omega\eta(q-m)]^2 = 0, \end{aligned} \tag{20}$$

where $\tilde{\varepsilon}$ is the dilatational elasticity and $\tilde{\gamma}$ the transverse one. η and ρ are the viscosity and density of the subphase, respectively. The capillary penetration length m is given by

$$m^2 = q^2 + i\omega\rho/\eta \quad \text{for } \mathrm{Re}(m) > 0, \tag{21}$$

Re(m) indicating the real part of m. The transverse and dilatational viscoelastic moduli can be written as

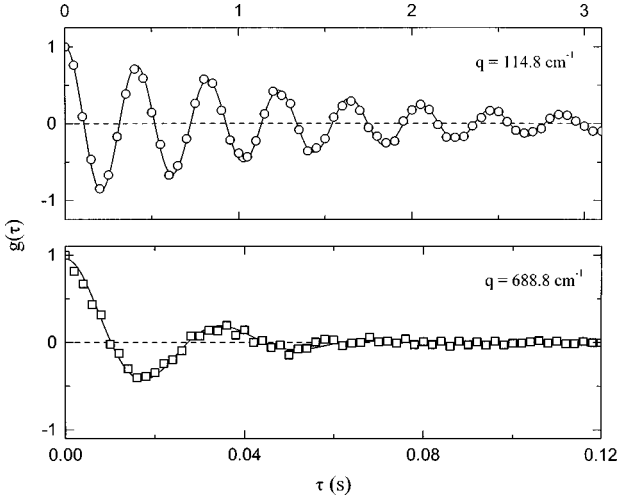

FIG. 16. Typical autocorrelation functions at low and high wave numbers for $\Gamma_s \approx 0.5\Gamma^{**}$ at 5 °C. The lines correspond to Eq. (23).

$$\tilde{\gamma} = \gamma + i\omega\mu, \quad \tilde{\varepsilon} = \varepsilon_R + i\omega\kappa, \tag{22}$$

where μ is the transverse shear viscosity and κ the dilatational viscosity. Capillary waves scatter light and the power spectrum of the scattered electric field by these hydrodynamic modes is given by [30]

$$P(\omega) = -\left(\frac{k_B T}{\pi\omega}\right) \mathrm{Im}\left[\frac{i\omega\eta(q+m) + \tilde{\varepsilon} q^2}{D(\omega)}\right], \tag{22}$$

Im(x) representing the imaginary part of x.

The Fourier transform of $P(\omega)$ gives the autocorrelation function $g(\tau)$. The experimental $g(\tau)$ have been fitted to a modified damped cosine function [32,33]

$$\begin{aligned} g(\tau) = {} & B - D\tau^2 + A_f \exp(-\Theta_f \tau) \\ & + A \exp(-\beta^2\tau^2/4) \exp(-\Theta\tau) \cos(\omega_0\tau + \phi). \end{aligned} \tag{23}$$

The term B-$D\tau^2$ accounts for the influence of possible long-wavelength vibrations that produce a droop in the correlation function at long times and arise from building vibrations. In general, in our data, this term has been negligible. The term $A_f \exp(-\Theta_f\tau)$ accounts for after pulsing effects. We have deleted the data of the first few channels of our correlator corresponding to times below 1 μs, thus this term is also usually negligible. The finite size of the laser beam and the solid angle subtended at the surface by the photomultiplier result in a finite wave-number range of capillary waves being illuminated. This instrumental broadening is accounted for by the Gaussian term $A \exp(-\beta^2\tau^2/4)$. The exponentially damped cosine term incorporates the damping Θ and the frequency ω_0 of the capillary waves. A phase factor ϕ is included to accommodate the experimental observation that the power spectrum is a skewed Lorentzian. Figure 16 shows a typical example of the quality of the fits for PVAC monolayers.

(b) Light-scattering results. For the sake of brevity we will discuss in detail only the results at one temperature: 5 °C; similar results were obtained at other temperatures. Table II shows the values of frequency and damping ob-

TABLE II. Frequency and damping coefficient of thermally excited capillary modes of PVAC monolayers at 5.3 °C and $\Gamma_s = 0.6$ mg m^{-2}.

q (cm^{-1})	ω_q (kHz)	Θ_q (kHz)	q (cm^{-1})	ω_q (kHz)	Θ_q (kHz)
114.8	15.35±0.03	0.68±0.03	459.2	122.24±2.0	23.2±6.0
114.8	15.61±0.03	0.67±0.04	459.2	123.30±2.0	23.1±2.0
229.6	43.50±0.20	3.66±0.10	459.2	124.73±2.0	23.2±2.0
229.6	43.25±0.14	3.69±0.30	574.0	150.20±6.0	38.8±5.0
229.6	43.38±0.08	3.74±0.20	574.0	156.75±3.0	34.1±4.0
344.3	80.07±0.40	10.8±1.5	688.8	183.50±2.0	47.3±4.0
344.3	79.38±0.50	11.3±0.5	803.6	198.43±2.0	60.8±9.0
344.3	79.16±0.60	10.3±0.7			

tained for the whole range of q. The different values for a given q correspond to experiments done on independently prepared monolayers with the same surface concentration ($\Gamma_s = 0.6$ mg m^{-2}) and provide an idea of the repetitivity of the whole experimental procedure. Figure 17 shows that the present results follow quite closely the expected q dependence for simple liquids (Kelvin's solution to the dispersion equation [30]) below 460 cm^{-1}, while the full solution of the theoretical spectrum is necessary for higher q's.

Earnshaw and McLaughlin [33] have discussed in detail how to obtain the four viscoelastic parameters from an experimental correlation function. However, since we are primarily interested in the dilatational properties, we have followed the approximate method of Yoo and Yu [17]. From the values of ω_0 and Θ we have calculated the maximum value of μ ($\mu_{\max}$) compatible with the observed damping at each q; the results are shown in Fig. 18(a). Harden and Pleiner have suggested that for a polymer film at the interface between two Newtonian fluids, both the transverse and the dilatational modes should be Maxwell-like at frequencies relevant for surface light-scattering (SLS) experiments [34]. Therefore, the μ values have been fitted to a Maxwell mode

$$\mu(\omega) = \gamma^0 \frac{\omega\tau_t}{1+\omega^2\tau_t^2}, \tag{24}$$

with $\tau_t = 2.04 \pm 0.12$ μs and $\gamma^0 = \mu_0/\tau_t = 6.8 \pm 0.1$ μN m^{-1}. Figure 18(b) shows the real part of the transverse elasticity, calculated from the previous results

$$\gamma(\omega) = \gamma_{\rm eq} + \gamma^0 \frac{\omega^2\tau_t^2}{1+\omega^2\tau_t^2}, \tag{25}$$

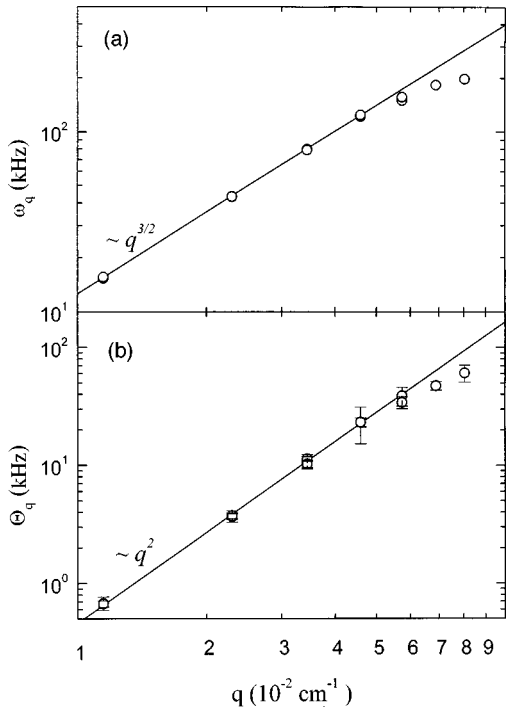

FIG. 17. Wave-number dependence of the characteristic frequency and damping constant for a monolayer with $\Gamma \approx 0.5\Gamma^{**}$. Notice that for $q < 460$ cm^{-1} the data closely follow Kelvin's equation, while the full solution of the dispersion equation is necessary for higher values of q.

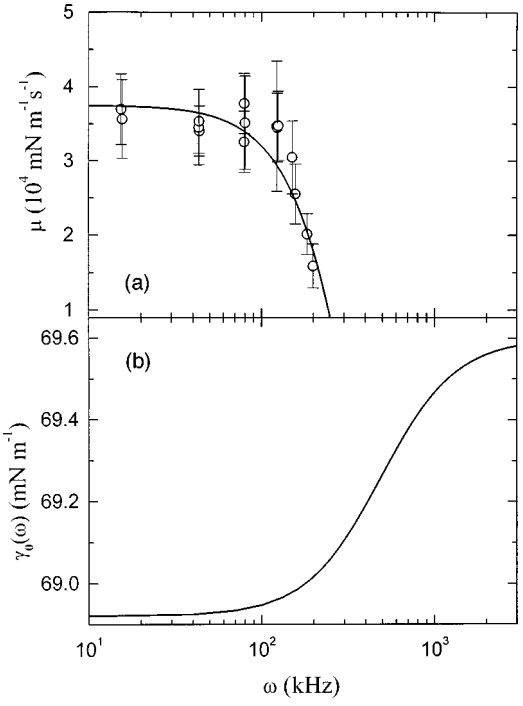

FIG. 18. (a) Frequency dependence of the maximum value of the transverse viscosity μ compatible with the damping at each q. The line represents a Maxwell mode (26). (b) Real part of the transverse elasticity (i.e., surface tension) γ calculated from a Maxwell mode with the amplitude and relaxation time fitted to the values of μ. Notice that below 100 kHz, γ is almost independent of frequency.

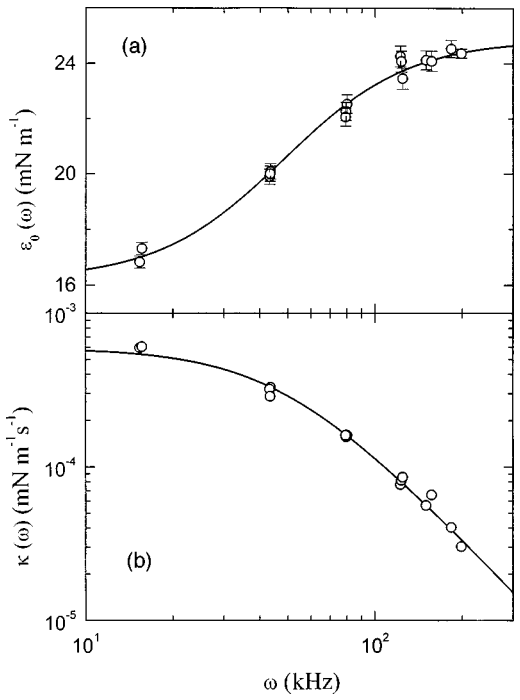

FIG. 19. Real and imaginary parts of the dilatational elastic modulus calculated from the SLS experiments with the μ values shown in Fig. 17.

with the value γ_{eq} taken from the equilibrium Π-Γ_s curve. It can be observed that below approximately 100 kHz, γ_0 remains constant and at the equilibrium value (68.9 mN m^{-1}) with a maximum deviation of 0.005 mN m^{-1}.

Using μ_{max} and $\gamma \approx \gamma_{eq}$, it is easy to obtain $\varepsilon(\omega)$ and $\kappa(\omega)$ from ω_0 and Θ. Figure 19 shows the results obtained as well

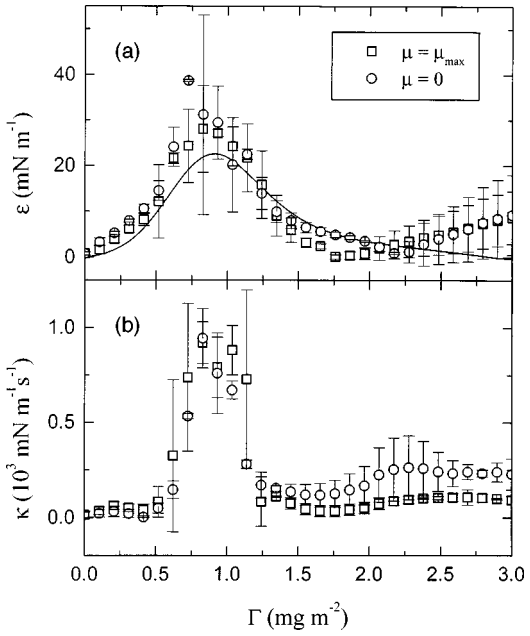

FIG. 20. Dilatational viscoelastic modulus for the monolayer at 25 °C and $q = 229.6\ \text{cm}^{-1}$, calculated from the autocorrelation functions and assuming for μ either its maximum value or zero. Notice that the differences in both cases lie within the experimental uncertainty. The continuous line in (a) represents the static elasticity obtained from Π vs Γ_s.

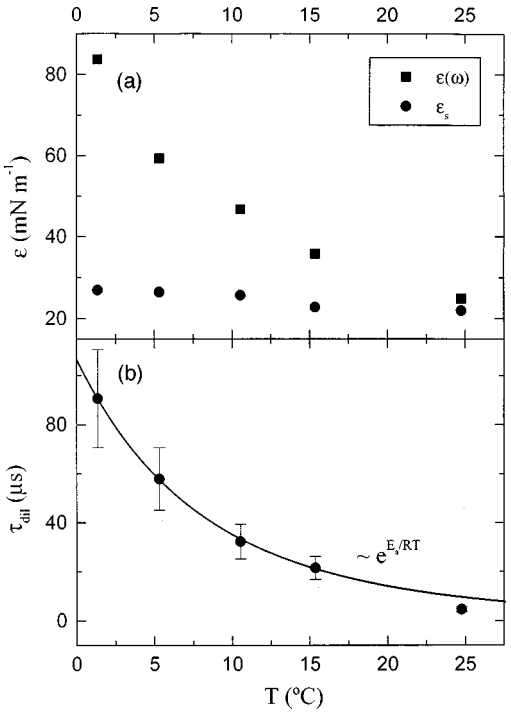

FIG. 21. (a) Comparison between static and SLS values of the real part of the dilatational elastic modulus for $\Gamma_s = \Gamma^*$ at different temperatures. (b) Temperature dependence of the relaxation time corresponding to the Maxwell mode from the SLS results. The line represents an Arrhenius-like temperature dependence.

as their fits to a Maxwell mode with $\tau_d = 25 \pm 1\ \mu$s and $\varepsilon_0 = \lim_{\omega \to 0} \varepsilon = 16.2 \pm 0.5$ mN m^{-1}. Even though the data extend beyond 100 kHz, the fit is quite good. It has to be considered to what extent the results shown in Fig. 19 depend upon the values of μ used. Figure 20 shows ε_R and κ for the 25 °C isotherm and $q = 229.6\ \text{cm}^{-1}$. Two sets of results have been calculated: one using $\mu = \mu_{max}$ as before and another one using $\mu = 0$. Only at surface concentrations well above Γ^{**} can one detect small differences between the two sets. Moreover, in both cases there is rather good agreement between the dynamic values of ε and the static values in this frequency range. Similar conclusions were reached at by Yoo and Yu [17] for the monolayer onto a subphase with pH = 7.0 and between 15 °C and 30 °C. Therefore, it seems reasonable to assume that the values obtained for the dilatational parameters are not very sensitive to those of the transverse ones. A detailed study of the viscoelastic behavior of the transverse modes could only be done by using Earnshaw and McLaughlin's method [33].

We have carried out similar experiments at different temperatures. As an example we will focus on the results corresponding to Γ^{**}. As can be observed in Fig. 21(a), there is a noticeable difference between the static and dynamic values of the elastic modulus. This might be due to the existence of an unrelaxed dilatational mode, as suggested by the spectral surface (Fig. 7) in which there is a shift of the dynamics towards short times as T is decreased. Assuming a Maxwell-type relaxation for this mode and considering that the dilatational viscosity is approximately constant within its uncertainty (see the discussion above), we have calculated the characteristic relaxation time for this mode. As is ob-

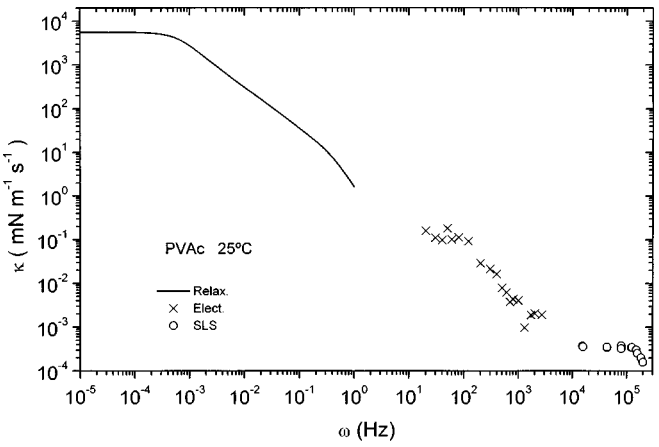

FIG. 22. Dilatational viscosity for a monolayer with $\Gamma \approx \Gamma^{**}$ as a function of frequency. Three relaxation regimes are visible through the ten-decade frequency regime.

served in Fig. 21(b), the temperature dependence of the calculated dilatational relaxation time τ_d can be described by an Arrhenius curve with activation energy $E_a = 86 \pm 7$ kJ mol^{-1}. This behavior clearly indicates that the dilatational viscosity strongly increases with decreasing temperature. The value of the activation energy is rather high, suggesting that the molecular motions are cooperative in nature.

It is important to notice that, as shown in Fig. 22, in the kilohertz range κ ranges from 10^{-5} to 10^{-3} mN m^{-1} s, while the results obtained in the step-compression experiments lead to values in the range $10^{0}-10^{4}$ mN m^{-1} s. Besides showing the good agreement between the data obtained using the different techniques, this figure shows that there are at least three well differentiated dynamic regimes as the frequency changes from the kilohertz to the millihertz range. These changes should be taken into account when obtaining equilibrium Π-Γ_s curves by continuous barrier movement and in transferring polymer monolayers onto solid substrates by the LB technique.

IV. CONCLUSIONS

The step-compression experiments show that the relaxation of the PVAC monolayers cannot be described by a single relaxation process. The use of regularization methods to analyze the results leads to complex relaxation spectra from which the real and imaginary components of the dilatational viscoelastic modulus can be easily calculated. The complexity of the spectra increases as the temperature decreases from 30 °C to 1 °C. The spectra agree with the predictions of the theoretical model recently proposed by Noskov, although for temperatures above 15 °C the agreement is not quantitative. The results of the oscillatory barrier experiments in the frequency range 0.1–1 Hz confirm those of the step-compression experiments. The dilatational viscosity κ is found to increase steeply with decreasing the frequency ω. In fact, a plot of $\ln(\kappa)$ vs $\ln(\omega)$ has a slope close to -1 in the frequency range $0.1-10^{-4}$ Hz. This value of the slope is close to that found for fluids between two solid surfaces.

The SLS experiments show that, in the kilohertz range, the dilatational viscoelastic modulus of the monolayer can be well described by a single Maxwell mode. As expected, the dilatational viscosity in this range is much smaller that in the millihertz range. In the intermediate region (20 Hz to 2 kHz) a single Maxwell relaxation mode is observed. It might be related to the adsorption-desorption dynamics of loops and tails out of the interfacial plane.

ACKNOWLEDGMENTS

This work was supported in part by Fundación Ramón Areces and by DGES under Grant No. PB96-609. F.M. was supported under by the FPI. We thank C.A.I. Espectroscopía for the use of its facilities.

[1] *Langmuir-Blodgett Films*, edited by G. Roberts (Plenum, New York, 1990).
[2] P. Krindel and A. Silberberg, J. Colloid Interface Sci. **71**, 39 (1979).
[3] M. R. Buhaenko and R. M. Richardson, Thin Solid Films **159**, 231 (1988).
[4] B. A. Noskov and T. U. Zubkova, J. Colloid Interface Sci. **170**, 1 (1995).
[5] M. Kawaguchi, Prog. Polym. Sci. **18**, 341 (1993).
[6] F. C. Goodrich, Proc. R. Soc. London, Ser. A **374**, 341 (1981).
[7] H. E. Gaub and H. M. McConnell, J. Phys. Chem. **90**, 6830 (1986).
[8] F. Monroy, J. Kahn, and D. Langevin, Colloids Surf. A (to be published).
[9] J. J. Jasper, J. Phys. Chem. Ref. Data **1**, 841 (1972).
[10] K. Ito, B. B. Sauer, R. J. Skarlupka, M. Sano, and H. Yu, Langmuir **6**, 1379 (1990).
[11] Y. Jayalakshmi, L. Ozanne, and D. Langevin, J. Colloid Interface Sci. **170**, 358 (1995).
[12] C. S. Gau, H. Yu, and G. Zografi, Macromolecules **26**, 2524 (1993).
[13] C. H. Sohl, K. Miyano, and J. B. Ketterson, Rev. Sci. Instrum. **49**, 1464 (1978).
[14] J. C. Earnshaw and R. C. McGivern, J. Phys. D **20**, 82 (1987).
[15] R. W. Richards, B. R. Rochford, and M. R. Taylor, Macromolecules **29**, 1980 (1996).
[16] V. Kolevzon and G. Gerbeth, J. Phys. D **29**, 2071 (1996).
[17] K-W. Yoo and H. Yu, Macromolecules **22**, 4019 (1989).
[18] R. Vilanove, D. Poupinet, and F. Rondelez, Macromolecules **21**, 2880 (1988).
[19] G. Loglio, U. Tesei, and R. Cini, J. Colloid Interface Sci. **71**, 316 (1979).
[20] P. Joos and M. Van Uffelen, Colloids Surf., A **75**, 273 (1993).
[21] A. E. Cardenas-Valera and A. I. Bailey, Colloids Surf., A **79**, 115 (1993).
[22] N. W. Tschoegl, *The Phenomenological Theory of Linear Viscoelastic Behavior* (Springer-Verlag, Berlin, 1989).

[23] J. Jakes, Collect. Czech. Chem. Commun. **60**, 1815 (1995).
[24] J. Krägel, G. Kretzschmar, J. B. Li, G. Loglio, R. Miller, and H. Möhwald, Thin Solid Films **248–285**, 361 (1996).
[25] G. Luengo, F.-J. Schmitt, R. Hill, and J. Israelachvili, Macromolecules **30**, 2482 (1997).
[26] G. Kretzschmar, J. Li, R. Miller, H. Motschmann, and H. Möhwald, Colloids Surf., A **114**, 277 (1996).
[27] B. A. Noskov, Colloid Polym. Sci. **273**, 263 (1995).
[28] J. D. Ferry, *Viscoelastic Properties of Polymers* (Wiley, New York, 1980).
[29] B. B. Sauer, Y. L. Chen, G. Zografi, and H. Yu, Langmuir **4**, 111 (1989).
[30] D. Langevin, *Light Scattering by Liquid Surfaces and Complementary Techniques* (Dekker, New York, 1992).
[31] L. Kramer, J. Chem. Phys. **55**, 2097 (1971).
[32] R. W. Richards and M. R. Taylor, J. Chem. Soc., Faraday Trans. **92**, 601 (1996).
[33] J. C. Earnshaw and A. C. McLaughlin, Proc. R. Soc. London, Ser. A **430**, 519 (1993).
[34] J. L. Harden and H. Pleiner, Phys. Rev. E **49**, 1411 (1994).